102nd European Study Group with Industry, University College Dublin, Ireland,
30 June – 4 July 2014

European Union
European Regional Development Fund
Investing in your future
A project supported by the INTERREG IVA Programme managed by the Special EU Programmes Body

TELLUS BORDER
Understanding Underground

GSI
Geological Survey of Ireland
Suirbhéireacht Gheolaíochta Éireann

Analysis and Interpretation of Tellus Border Electromagnetic Data

Problem submitted by the Geological Survey of Ireland

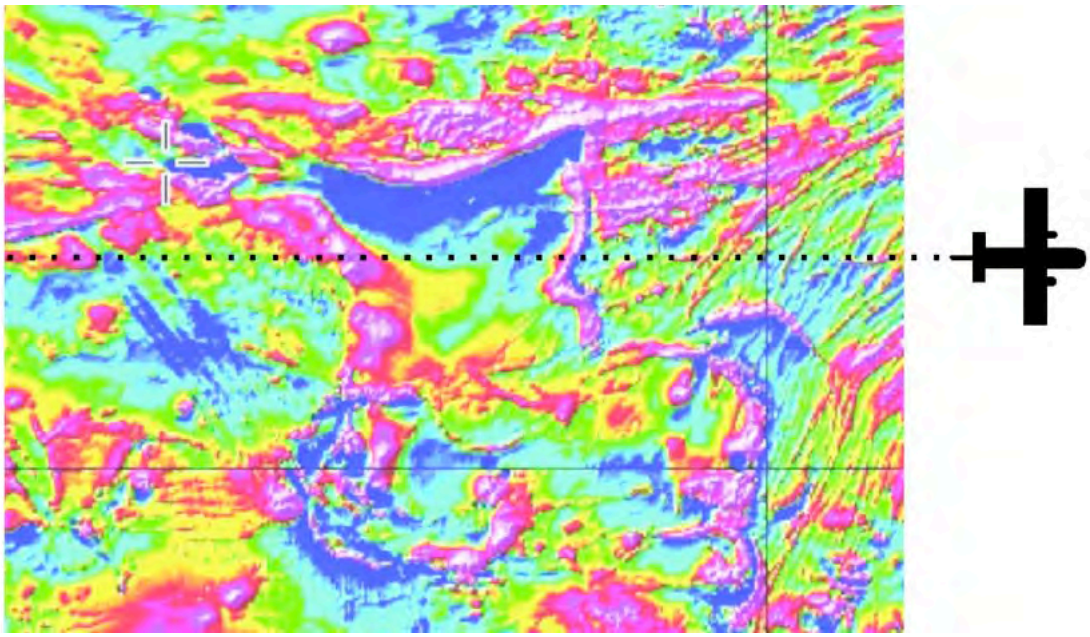

Study group:

Dr Eugene Kashdan, UCD
Dr Avril Hegarty, MACSI, UL
Dr Andrew Parnell, UCD

Dr Davide Cellai, MACSI, UL
Dr Silvia Gazzola, University of Padova
Mr Andrew Gloster, UCD
Mr Ali Faqeeh, MACSI, UL
Mr Allan S. Nielsen, EPFL
Mr Kevin O Sullivan, MACSI, UL

Inquiries and additional information

Statistical modeling and data analysis:

Dr Avril Hegarty, avril.hegarty@ul.ie;
Dr Andrew Parnell, andrew.parnell@ucd.ie

Electromagnetic data interpretation and inversion:

Dr Eugene Kashdan, ekashdan@maths.ucd.ie

General inquires:

Dr Eugene Kashdan, ekashdan@maths.ucd.ie

Problem statement

Background

The collection of airborne electromagnetic (EM) data is a common surveying technique used to assist geologists to interpret subsurface geology, structure, mineralization and contamination. Airborne EM surveying is an induction technique where a known current is circulated in a coil (transmitter) and the response of the earth to this current is measured in another coil (receiver) both coils are housed within the aircraft. EM surveys are commonly carried out in either the frequency domain (where the effects are measured at different frequencies) or in the time domain (where the effect of the current in the earth is measured at different times when the transmitting current is turned off). The former are often referred to as FEM while the latter are often referred to as TEM. In the case of FEM, two parameters for each frequency are measured, the in-phase component P and the out of phase (or quadrature) component Q. The measurements are given in ppm (parts per million) of the transmitted field strength (measured in V or more commonly mV). Apparent resistivity, or its inverse apparent conductivity, and apparent depth can be calculated from these data which are more readily amenable to interpretation of the data in terms of geology, etc.

The Geological Survey of Ireland (GSI) along with the Geological Survey of Northern Ireland (GSNI) carried out a FEM survey over six counties in Ireland close to the border with Northern Ireland. The project is part of a larger project funded by the EU (INTERREG IVA) and known as the **Tellus Border** project.

Measurements were collected at four different frequencies (approximately 0.9, 3, 12 and 25kHz). Prior to presenting the data the raw data is corrected for many factors, including altitude, temperature, instrument drift, etc.

The interpretation of this data is commonly carried out using specialist software packages where the data is used to produce resistivity models of the subsurface. These models are then interpreted in terms of rock types, their boundaries with one another, and other features such as mineralization or contamination. However, solutions are non-unique and it is helpful to have some a priori knowledge of the area being studied. Such information may come from outcrops, drill holes with depths to particular geological units, or physical property data such as the electrical resistivity of the different rock units. For each data point a 1D model can be determined which comprises resistivity variations

with depth (down to a depth of about 50 to 60m in the case of the survey carried out by the Tellus Border project). The resistivity estimate is used to interpret (assign a rock type) the geological nature of the earth. This can be aided (constrained) by known rock units in the region.

Problem to be addressed

When GSI, GSNI and its geophysical contractors and consultants have attempted to carry out interpretations of the EM data it has not been possible to develop sensible models. We have identified some issues: (i) Strong peaks of signal at the low-frequency readings, apparently correlated spatially but not due to human activity. (ii) Regions of high spatial variability of low-frequency readings, which look like noise.

Questions

GSI asks the European Study Group with Industry:

1. Determine if the FEM data can be used to obtain a sensible and robust resistivity model so that the data can be used to aid the geological interpretation of the subsurface.
2. Develop approaches that can be used routinely to develop such models.
3. What is the relationship between altitude, frequency and P & Q values?
4. Which frequencies can be used to give good data based on altitude and ground resistivity?
5. Can uncertainty be assessed?
6. How do we deal with noise without losing geological information?

Contents

Chapter 1

Summary and recommendations

1.1 Brief answers

Here we summarise the answers to the questions posed by the GSI. The detailed analysis and corresponding discussions are provided in the subsequent sections.

1. Based on our analysis of the test-line data we conclude that the FEM data can be used for geological interpretation of the surface albeit with a number of limitations.

2. The quasi-1D model is fast and robust tool for data interpretation (inversion). Following its calibration with the ground tests, this model could be used for initial assessment of data and analysis of its quality. The full 3D solver should be developed based on the forward modeling combined with the nonlinear optimization.

3. The in-phase P and quadrature Q components are depending (non-linearly) from both altitude and frequency. The dependence is detailed as part of the computational algorithm in Section 4 (Data Interpretation). Under assumptions, made in this section, the values of both P and Q are decaying exponentially with growth in altitude h. Considering that the noise level remains the same, increasing altitude leads to the lower signal-to-noise ratio and as a consequence to less accurate results. The values of P and Q that are non-physical could be ignored and replaced with the interpolated values from the neighboring points.

4. Despite their lower penetration depth, the higher frequencies provide the most reliable data due to their better signal-to-noise ratio (SNR). If the survey plane can fly on the low altitude, the lower frequencies can be used. This analysis concentrated on the resistivity results and for 900Hz and 25kHz, it seems that flying lower provides more replicable results. For 3kHz it doesn't seem to make much difference provided you fly below 90m. For 12kHz they were all pretty much the same. Results for the Qs were similar. For the Ps, the best altitude appears to be around $73m$, but the lowest altitude gives fairly similar results in all cases except 'P12'

where one flight had very odd results. **As an overall conclusion, we recommend flying at as low an altitude as possible**. However, we do not quantify the bias in the measurements. Thus it is possible that flights taken at the lowest altitude also contain considerable bias, and that a higher altitude may be preferable when considering both issues simultaneously.

5. The uncertainty can be quantified as part of the forward data interpretation model and assessed both analytically and numerically over the section of the test line that has corresponding ground measurements.

6. The Bayesian noise estimation algorithms could be applied to the data for both analysis and correction properties. From our study follows that the contractor did a very consistent work in noise removal from the measured data. It is clearly visible in the analysis of the resistivity measured on the test line. Finally, the inversion algorithm could be tested by adding different levels of random noise to control replicability of the results.

1.2 Possible extensions of the project

We have a number of suggestions that could be considered and explored further. While some of them require additional funding from either public or private organisations, the number of ideas could be realised without additional financial expenses from the GSI. We expect that this work will yield joint publications in the peer-reviewed scientific journals.

- A UCD MSc Statistics student could do further analysis on the data as their project at no cost to GSI. However, additional data would be required.

- A UCD Theoretical Physics student can continue work on the quasi-1D model in order to achieve better calibration with the ground measurements and analyse both uncertainty and the effect of the noise in the measured data also with no cost to GSI. The existing code could be ported on the GPU-powered cluster (a recent addition to the computational resources of the Dr Kashdan's group). This may yield better accuracy and resolution of the inversion algorithm.

- A PhD or postdoctoral researcher could do further extensive research, with a duration of between 6 months and 4 years. There would be the possibility of this being funded by a grant from Enterprise Ireland or similar. This work can include development and implementation of the 3D frequency domain inversion code, inversion of the time-dependent EM data, and/or detailed statistical analysis of both frequency- and time-domain datasets using modern statistical techniques such as cluster analysis and functional data analysis.

- Consultancy work by the senior investigators: Avril Hegarty and Andrew Parnell (statistical data analysis) and Eugene Kashdan (forward and inverse electromagnetic modeling and data interpretation) with possible involvement of other members of the group.

Chapter 2

Analysis

2.1 Introduction and summary

In this chapter we analyse Tellus test-line flights at similar altitudes to determine which are most replicable. The stages involved in this analysis are:

1. An initial data clean-up stage to remove flights that went off course, and areas of the testline where data were recorded over water.

2. An exploratory data analysis to determine which variables are important and to reveal any hidden structure in the data

3. A statistical model to quantify the variability between test flights that took place at the same target altitude

The sections below correspond to each of these steps. A short 300m ground-based test line covering part of the flight testline, of actual resistivity measurements was available. However these data were not satisfactory to examine the potential bias described below, so we do not discuss it further.

For brevity, we concentrate on analysing the resistivity values. Further analysis performed on the P and Q values gave identical conclusions. As will be shown below, in nearly all cases the flights that were most replicable were those where the aircraft was aiming to fly at the lowest altitudes. This suggests that future flights to determine resistivity should also be conducted at the lowest feasible altitude. Note, however, that we do not quantify the bias in the resistivity in this document. Thus it is possible that flights taken at the lowest altitude also contain considerable bias, and that a higher altitude may be preferable when considering both issues simultaneously.

2.2 Data cleaning

The data we use come from the file `GSI_TESTLINE_1_5_240614.csv`. Data are given along a 6 km. test line with readings taken every 0.1 second or approximately every 6 metres. One end of the test line, for approximately 1 km, was over the sea. There were 5 individual flights on different days and each of these flew up and down the line changing altitude after each turn to give 7 different altitudes. The key variables in the file are:

- 'LINE' which contains the flight number and the replicate
- Location variables 'X_IRISH_NG' and 'Y_IRISH_NG' which contain the coordinates of the current measurement
- 'Laser' which contains the current altitude. Note that although a target altitude is set fluctuations are unavoidable. Hereon we refer to the target altitude as the mean of the variable 'Laser' for that particular set of flights
- Variables starting with 'P', 'Q' and 'Res' which give the frequency values at the different frequencies '09', '3', '12' and '25'. As previously stated in this document we analyse the 'Res' values in this report and discuss the results from the 'P' and 'Q' values briefly in the Results section.
- 'Dist' which contains an estimate of the distance along the transect.

A plot of the location variables (Fig 2.1) shows that the transect they took was highly similar except in a few places at the ends where they went slightly off-course. Further examination of the dataset reveals that the first flight (L7001) at all 7 altitudes started and finished 500 metres further along the testline than the other 4 flights. Furthermore, a large number of the measurements in the data set occur over the sea or at locations which are far from the testline where the plane may have been blown slightly off-course. We removed all these variables (shown in red in Figure 2.1). As a final step, we standardised the distance variable to 10m steps so that each flight/altitude combination had approximately 450 readings for each P, Q and Res variable. The final data set we use has 25,417 observations, as opposed to the 34,898 available in the original data set.

As a final correction we found the variables 'flight' and 'Line' to be very confusing. The dataset contains 5 flights at which 7 different altitudes were attempted. We have re-phrased this to say that there were 7 different flights of which there are 5 replicates of each altitude. This makes the subsequent modelling easier to follow as then each flight number refers to the same altitude attempt. We can thus quantify experimental variability a bit better.

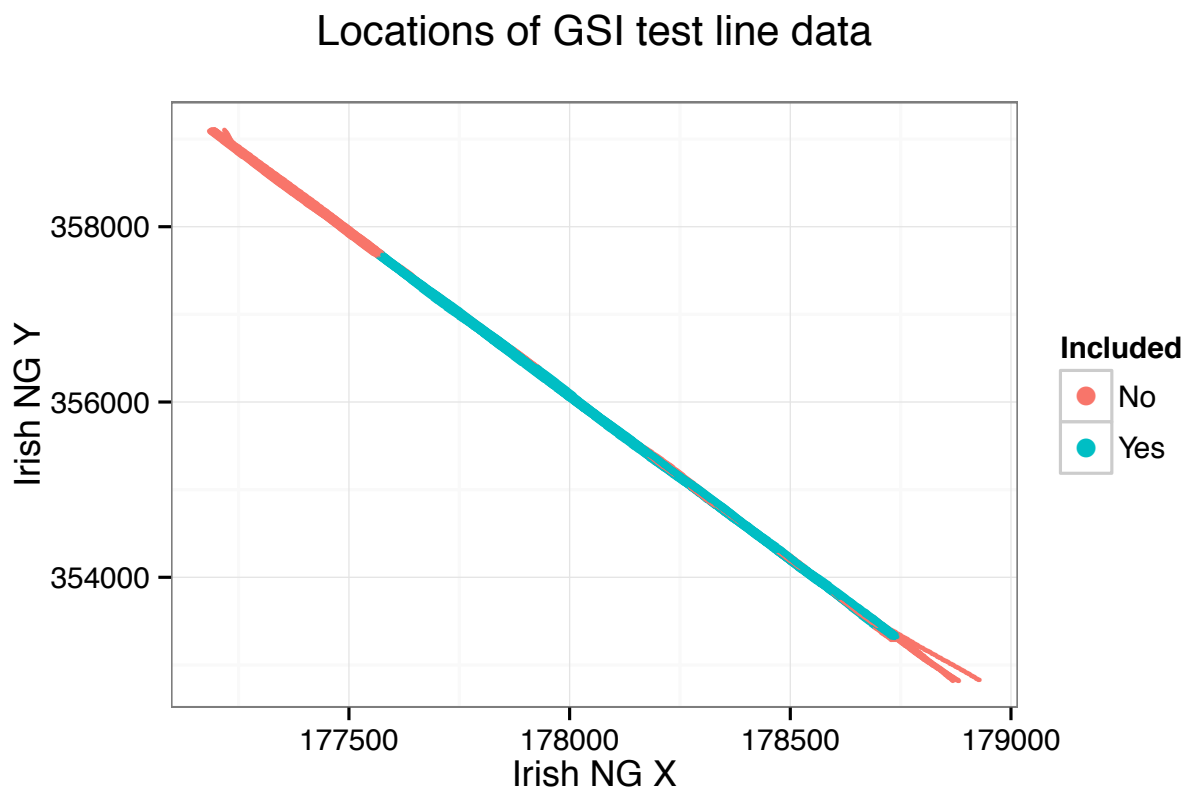

Figure 2.1: Locations at which the test line data were obtained. Data points marked in red were removed from the analysis as they did not provide for measuring replicability

2.3 Exploratory data analysis

2.3.1 Weather

We examined the weather records for the days of the flights to see if this might have had an impact on the results. However, none of the days showed particularly strong wind (the windiest day had just a moderate breeze), nor excessive rainfall in the 3-days prior to the flight, nor unusually high or low temperatures. See Figure 2.1.

Flight	Date	Station	Rain (mm)	Max Temp °C	Min Temp °C	Mean Wind (knots)
L7001	26/10/2011	Finner	0.3	11.0	4.5	9.8
L7025	10/12/2011	Finner	7.4	8.6	2.9	12.8
L7050	23/01/2011	Finner	2.9	8.4	3.7	10.7
L7129	08/05/2011	Finner	2.2	11.1	2.4	7.9
L7177	15/07/2011	Finner	1.9	16.2	9.6	9.1

Table 2.1: Weather Reports (source: Met Éireann)

2.3.2 Power Lines and Built-up Areas

Examination of the test line showed that there were no major power lines crossing it which might have affected the results. However there is some suggestion in some of the resistivity plots of anomalies at about 2km and 5km. The former of these corresponds to a main road and the latter to the built-up area of Uragh. A map of the testline is given in Figure 2.2.

2.4 Statistical modelling

The objective of this section is to build a statistical model for each flight's resistivity and quantify the variability between the different altitude replicates. We model the resistivity for each frequency in turn and assume that the true resistivity lies roughly as the mean of the different resistivity values. We assume that resistivity changes smoothly over the transect in question so we modelled these as a Brownian motion. A plot of the different resistivity values for two particular frequencies is shown in Figure 2.3.

The key unknown parameter in our statistical model measures the variability of the different runs at the same target altitude irrespective of the distance along the testline. We call this value the 'replicate variability' and calculate it for each frequency and target altitude. Figure 2.4 shows the output of these runs. From looking at these plots we can draw the conclusion that lower target altitudes provide resistivity values that are more similar to each other.

The remaining paragraphs of this section outline the statistical model, and can be skipped for those who are not interested in technical detail. Let $y_j(d)$ be the log resistivity values for a certain frequency along transect distance d on replicate j. We define a state space model with random effects such that:

$$y_j(d) = \mu(d) + b_j + \epsilon_j(d)$$

where $\mu(d) \sim N(\mu(d - \Delta d), \sigma_\mu^2 \|\Delta d\|)$ is a Brownian motion, $b_j \sim N(0, \sigma_b^2)$ is the additive random effect of each replicate, and $\epsilon_j(d) \sim N(0, \sigma^2)$ is a model error term. The key parameter here is σ_b; our replicate variability. The model is a little bit simplistic seeing as the different replicates are unlikely to be a simple shift of the mean. Thus a more realistic model might have b as a function of d too.

We first fitted the above using the Bayesian Hamiltonian Monte Carlo package 'stan' using half-Cauchy weakly informative priors on the standard deviation terms σ_μ, σ_b and σ. We ran the model

Figure 2.2: Map of flight testline

for each of the flights at each of the 4 different frequency values (Res09, Res3, Res12 and Res25), totalling 28 model runs. We ran each for 1000 iterations which meant that the computing took about 12 hours, and checked for convergence using the standard Brooks-Gelman-Rubin statistic.

2.5 Results and Conclusions

Figures 2.3 shows the different replicate data (in colour) and overall mean estimate (μ; in black) for two examples, one where the replicated variability is likely to be low and one where it is high. There are a total of 28 of these plots of which we only show two. However, for each run we have a single estimate of σ_b, our replicate variability. Recall that a small σ_b indicates an altitude at which the runs are most repeatable. We can compare these for different frequencies and different target altitudes. Figure 2.4 shows all of them.

For 900Hz and 25kHz, it seems that flying lower provides more replicable results. For 3kHz it doesn't seem to make much difference provided you fly below 90m. For 12kHz they were all pretty much the same. As a further part of the analysis, all of the models were rerun on the 'P' and 'Q' values. Graphs of these are available if required. The same conclusion holds for the 'Q' frequencies - fly low. For the 'P' values, the best altitude appears to be around 73m, but the lowest altitude gives fairly similar results in all cases except 'P12' where one flight had very odd results. As an overall conclusion, we recommend flying at as low an altitude as possible.

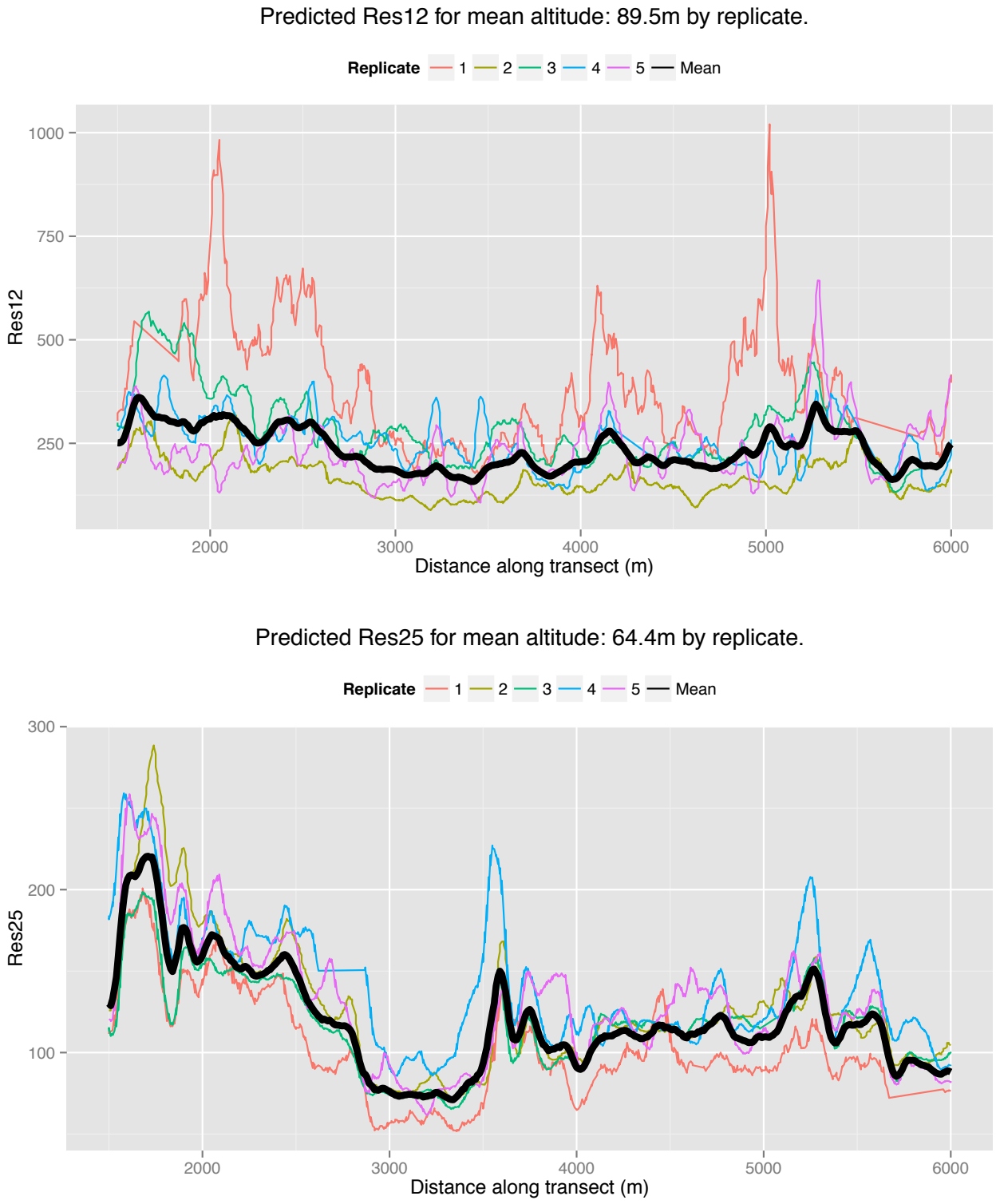

Figure 2.3: Plots of resistivity values (y-axis) against distance along transect (x-axis). The individual lines represent the raw resistivity values (here at frequencies 12KHz and 25KHz) for each replicate. The top plot was obtained at the target altitude of 89.5m, whilst the bottom plot at 64.4m. The black line represents the modelled mean in resistivity created via the state space model detailed in this section. Our key parameter measures the variability of these coloured lines around the black mean. In these two plots it appears that the lower altitude mean (bottom plot) has less variability around it than the higher altitude (top plot).

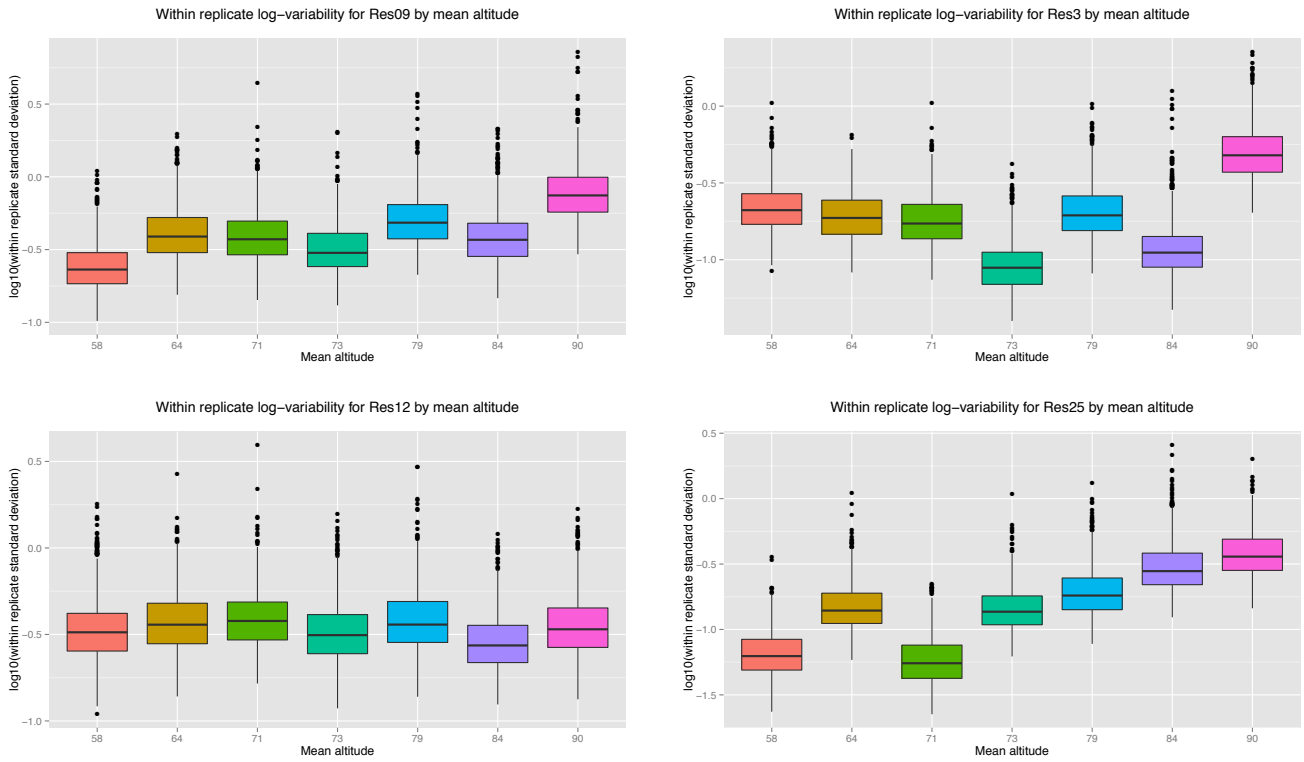

Figure 2.4: Boxplots of the log of the replicate variability (y-axis) versus the target altitude (x-axis) for the four different frequencies based on resistivity values. These are the main output of the state space model detailed in Section 2.4. Lower values indicate that there is less variability between the replicates. For both the 900Hz frequency and 25KHz frequency it lower altitudes seem strongly desirable. This is less clear however at frequencies 3KHz and 12KHz. Re-creating the same plots for P and Q values yields similar answers.

2.6 Further Work

In this section we outline possibilities for further collaboration. These include:

1. Quantifying the possible bias mentioned in Section 1 such that the accuracy of the resistivity results could be calculated. This would require ground-based measurements for a suitably long test-line

2. Further investigation of the problem of "spikes" in the dataset. Cluster analysis or product partition models for example, could be used to analyse these to try to establish whether the spikes are due to real phenomena e.g. power lines, or are just noise.

3. Expansions to the random effects state space model. We could, for example, quantify whether the replicate variability changes along the transect, or try and 'borrow strength' between the different frequencies by modelling them simultaneously. An alternative approach would be to consider the data as functions and use functional data analysis approaches. Preliminary exploratory analysis using this approach gave very similar results, but with potential to smooth the data. None of this requires further data to complete the analysis.

4. The similar analysis could be also applied to the time-dependent data from the recent survey

Chapter 3

Interpretation

3.1 Introduction

A number of interpretation methods exist for aerial electromagnetic (EM) data that are designed to provide images that mimic the distribution of the true parameter(s) in the geologic section. Generally, the methods fall into two classes: (1) direct transform of data to a generalized model such as a half-space, and (2) inversion of data to a specific model such as a layered earth, where a starting model is employed, followed by iterative fitting of the data to yield a best fit in the least-squares sense.

There are two types of the EM measurement techniques: time-domain (TEM), where measurements are done as a function of time and frequency domain (FEM), where measurements are done at one or more frequencies. The survey that we analyzed was done using the FEM approach.

Below we give a brief survey of the existing methods for FEM data interpretation in accordance with [1].

Transform methods ([2, 3]) have the advantage of yielding a single robust solution for the given output parameter, and the disadvantage that the output parameter may provide a poorly resolved image of the geology.

Inversion methods (e.g., [4, 5]) have the advantage of yielding much superior resolution for the given output parameter and the disadvantage that the output parameter may vary with the starting model, so this lack of robustness is always a concern when evaluating an interpretive output.

Inversion methods for the interpretation of EM data for a layered earth are being employed more commonly for airborne surveys as the data quality is improved and as both the number of frequencies and computer speed are increased. Numerous papers have been published on the methods used to invert for the resistivity of a layered earth model under the assumption that the magnetic permeability and dielectric permittivity are the same as those of free space (see, for instance, [6, 7, 8]).

In basis of the methods discussed above lies a quasi-1D approach. It is often argued that 3D inversion

of entire airborne electromagnetic (AEM) surveys is impractical, and that 1D methods provide the only viable option for quantitative interpretation. However, real geological formations are 3D by nature and 3D inversion is required to produce accurate images of the subsurface. With increasing computational power and advance of numerical techniques it is getting practical to invert entire AEM surveys to 3D conductivity models with hundreds of thousands if not millions of elements [9, 10]

The principles of the EM surveying could be summarized as follows:

- The EM field is generated by passing an AC through a wire coil (transmitter)
- EM field propagates above and below ground.
- If there is conductive material in ground, magnetic component of the EM wave induces eddy currents (AC) in conductor.
- The eddy currents produce a secondary EM field which is detectedby the receiver.
- The receiver also detects the primary field (the resultant fieldis a combination of primary and secondary which differs from the primary field in phase and amplitude).
- After compensating for the primary field (which can be computed from the relative positions and orientations of the coils), both the magnitude and relative phase of the secondary field can be measured.
- The difference in the resultant field from the primary provides information about the geometry, size and electrical properties of the subsurface conductor.

Remark: The resistivity derived from the airborne EM data, based on a nonmagnetic earth, is not reliable in highly magnetic areas but this topic is beyond the scope of the report.

3.2 Forward modeling

For our work we assume that in the close vicinity of the measurement point earth could be represented as a layered medium. The combination of the measurement points forms a grid that corresponds to the area below the testlines. The neighboring grid points are interpolated to give information about the subterranean structures.

The geometry of the problem is shown in Fig. 3.1 The airborne transmitting and receiving coils are arranged in a horizontal coplanar orientation. For purposes of an inversion, the sensor height h is assumed to be known from a radar or laser altimeter, and the dielectric permittivities are ignored for all layers. The distance between the coils r is fixed. The frequencies of 912, 3005, 11962 and 24510 Hz are used for the computation of the in-phase P and quadrature Q components that in turn are used as an input for the inversion.

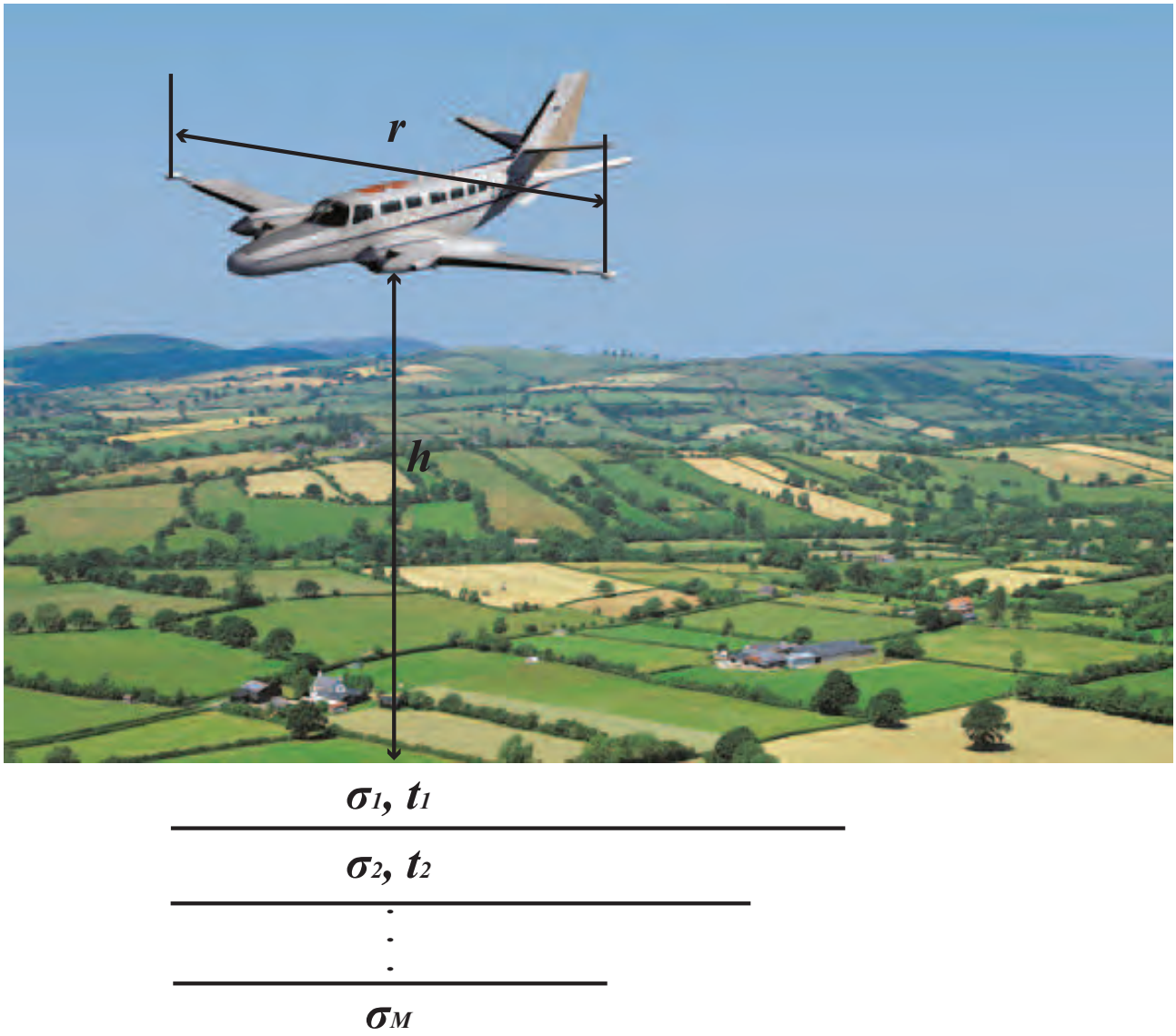

Figure 3.1: The geometry of the EM coplanar coil system over a M-layer earth.

The EM response of a layered half-space for dipole source excitation is given in [11, 12, 13] among others. If a horizontal coplanar system is at a height h above the layered halfspace, the secondary magnetic field H_s, normalized against the primary field H_0 at the receiving coil, is

$$[P + iQ]_{\times 10^{-6}} = \frac{H_s}{H_0} = r^3 \int_0^\infty R(\lambda)\lambda^2 \exp(2u_0 h) J_0(\lambda s) d\lambda \tag{3.1}$$

where r is the coil separation, λ is the variable of integration, and J_0 the Bessel function of the first kind of order zero. The values of P and Q in the dataset are given in ppm and translated into their

original values. The term $R(\lambda)$ can be written as

$$R(\lambda) = \frac{Y_1 Y_0}{Y_1 + Y_0} \tag{3.2}$$

where $Y_0 = u_0/i\omega\mu_0$ is the intrinsic admittance of free space, Y_1 is the surface admittance, i is the square root of -1, ω is the angular frequency, μ_0 is the magnetic permeability of free space, and u_0 is equal to $\sqrt{\lambda^2 + k_0^2}$, where k_0 is the wave number of free space. For a M-layer earth, Y_1 can be obtained by the following recurrence relation:

$$Y_m = \hat{Y}_m \frac{Y_{m+1} + \hat{Y}_m \tanh(u_m t_m)}{\hat{Y}_m + Y_{m+1} \tanh(u_m t_m)}, \qquad m = 1, 2, \ \ldots, \ M-1, \tag{3.3}$$

where

$$\hat{Y}_m = \frac{u_m}{i\omega\mu_0\mu_m} \tag{3.4}$$

and

$$u_m = \sqrt{\lambda^2 + k_m^2} \tag{3.5}$$

where k_m is the wave number of m-th layer given by

$$k_m = \sqrt{i\omega\sigma_m\mu_0\mu_m - \omega^2\varepsilon_0\mu_0\mu_m} \tag{3.6}$$

and where t_m is the thickness, μ_m is the relative magnetic permeability, σ_m is the conductivity of the m-th layer, and ε_0 is the dielectric permittivity of free space. In practice, the reciprocal of the conductivity, the resistivity ρ_m, is commonly used. In our model we also make the number of additional assumptions. First we consider that the subterranean medium is not magnetic $\mu_m = 1$ for all layers and, second, since we employ the quasi-static assumption, equation (3.6) becomes

$$k_m = \sqrt{i\omega\sigma_m\mu_0}. \tag{3.7}$$

In the half-space at the bottom of the electrical section,

$$Y_M = \hat{Y}_M. \tag{3.8}$$

Y_1 is a complex function of an integral variable λ, the angular frequency ω, the magnetic permeability μ, the conductivity σ (or the resistivity ρ), and the thickness t of the layers. For a given model, Y_1 can be calculated by using the recurrence relationship in equations (3.3)(3.5). Then, Y_1 can be substituted into equations (3.2) and then into (3.1) to yield the responses of the system over the model.

The recursive approach to computing reflection coefficient R of the multilayer system corresponds to the so called *Transfer Matrix Method* (TMM) [14]. TMM is often employed to compute the signal transmittance of the multilayer quasi-1D structures, like multilayer thin films.

3.3 Inversion

3.3.1 General background

Inversion of EM data requires that accurate frequency relationships are preserved in the data, which can be impacted by:

- Instrument calibration errors
- Leveling errors
- Primary field removal
- Random noise (temperature effects, airplane movement)

In our analysis we considered the raw P and Q measurements. In cases, where the measurements were considered "non-physical" we applied linear interpolation to obtain the values of P and Q from the neighboring points. This approach has its pros and cons. From one side it is prone to the effects mentioned above on the data. However, on the other side, filtering/smoothing data yields the loss of valuable information, which is supposedly small, but is also very difficult for quantification.

Remark: The resistivity values provided by the contractor are estimated with the factors mentioned above taken into account.

In order to invert the data and compute the subterranean conductivity we used the model-oriented inverse problem approach. The goal of this approach is to fit the measurement data with the forward model using the constrained nonlinear optimization.

Measurement data fit with the modeled results to minimize the residual (Tikhonov parametric functional $P^\alpha(\sigma)$):

$$P^\alpha(\vec{\sigma}) = \|\vec{F}(\vec{\sigma}) - \vec{d}\|^2 + \alpha\|\vec{\sigma} - \vec{\sigma_b}\|^2 \to min, \tag{3.9}$$

where $\vec{F}$ is a forward operator, $\vec{\sigma}$ is the vector of M conductivities, $\vec{d}$ is the vector of measurements of length N and $\vec{\sigma_b}$ is the vector of *a priori* conductivities. For computational purposes conductivities could be replaced with the resistivities to avoid loss of significant digits.

3.3.2 Model parameters and settings

According to the company that did a survey, we set the distance between the coils $r = 21.38m$. The height h and raw (unfiltered) P and Q values are downloaded from the testline data file.

The initial setting is average resistivity $\rho = 200\Omega \cdot m$ is sufficient for the upper soil and rock.

The resolution in depth is $2.5m$. The conductivity (resisitivity) at each point on the computational grid is computed for all frequencies in accordance with their skin depth L is given by

$$L = \sqrt{\frac{2}{\omega\sigma\mu}} \approx \frac{503}{\sqrt{f\sigma}}, \tag{3.10}$$

where f is a given frequency.

Frequency, Hz	**Skin depth,** m
912	235
3005	130
11962	65
24510	45

Table 3.1: Skin depth for different frequencies used in the survey. Based on $\sigma = 0.05S/m$

Skin Depth is the depth at which the amplitude of a plane wave has decreased to $1/e$ or 37% relative to its initial amplitude. We use a skin depth as an indicator of reliability of the measurements for each frequency: the SNR below the skin depth is too low and the results are probably not trustworthy.

At the same depth all frequencies should correspond to the same values of the conductivity (resisitivity). The results are not very reliable far from the surface however, they could give a good estimation of the subterranean structures on the depth up to 45m (where at least three frequency return sensible results).

In our simulations, we applied the Levenberg-Marquardt algorithm often employed in EM inversion [15]. The cost function that we minimize consists of two parts: fitting the forward model with P and Q measurements and a requirement that the conductivities (resisitivities) within the same depth, controlled by the skin depth of each frequency, remain the same (e.g., if the skin depth of the frequency 24510Hz is 45m then the conductivity/resistivity reconstructed within this depth should be the same for three other frequencies).

3.3.3 Validation of the approach

.

The results in Figs. 3.2 and 3.3 give an initial picture of the reconstructed properties of the subterranean structures along the test line 7001. The flight starts over the sea, so the first 99 points in the dataset that correspond to approximately 530m flown by the surveying plane are removed from the calculations.

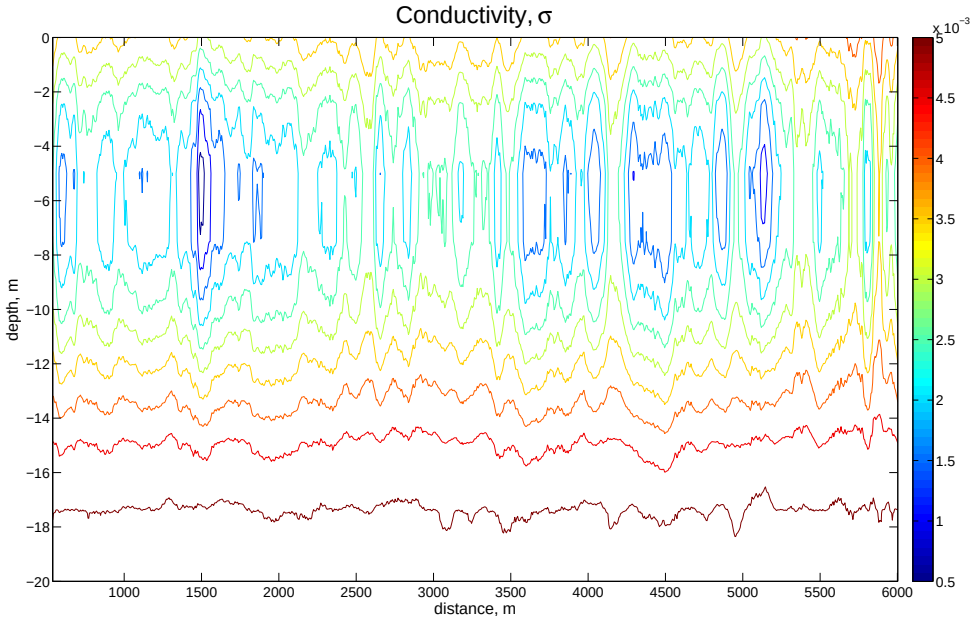

Figure 3.2: Reconstruction of conductivity

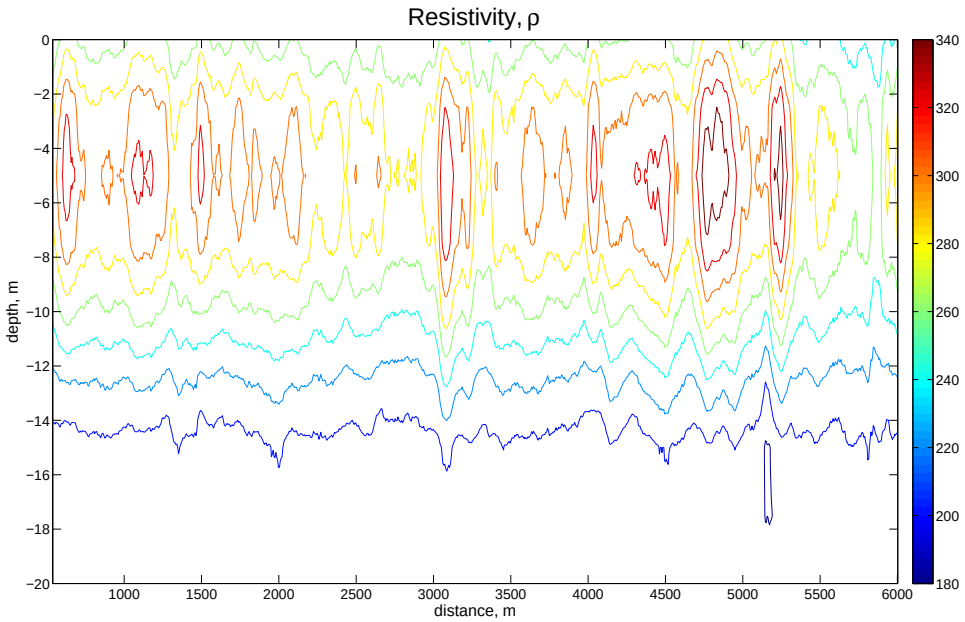

Figure 3.3: Reconstruction of resistivity

The optimization algorithm yields sensible results till approximately 25-30m depth. The sensitivity of the algorithm can be improved by the increasing the absolute and relative tolerance of the calculations of the integral (3.1). However, it also yields a significant increase in the computational time.

The following plots show qualitative comparison between ground measurements of resisitivity and the resistitivity reconstructed for approximately same part of the testline.

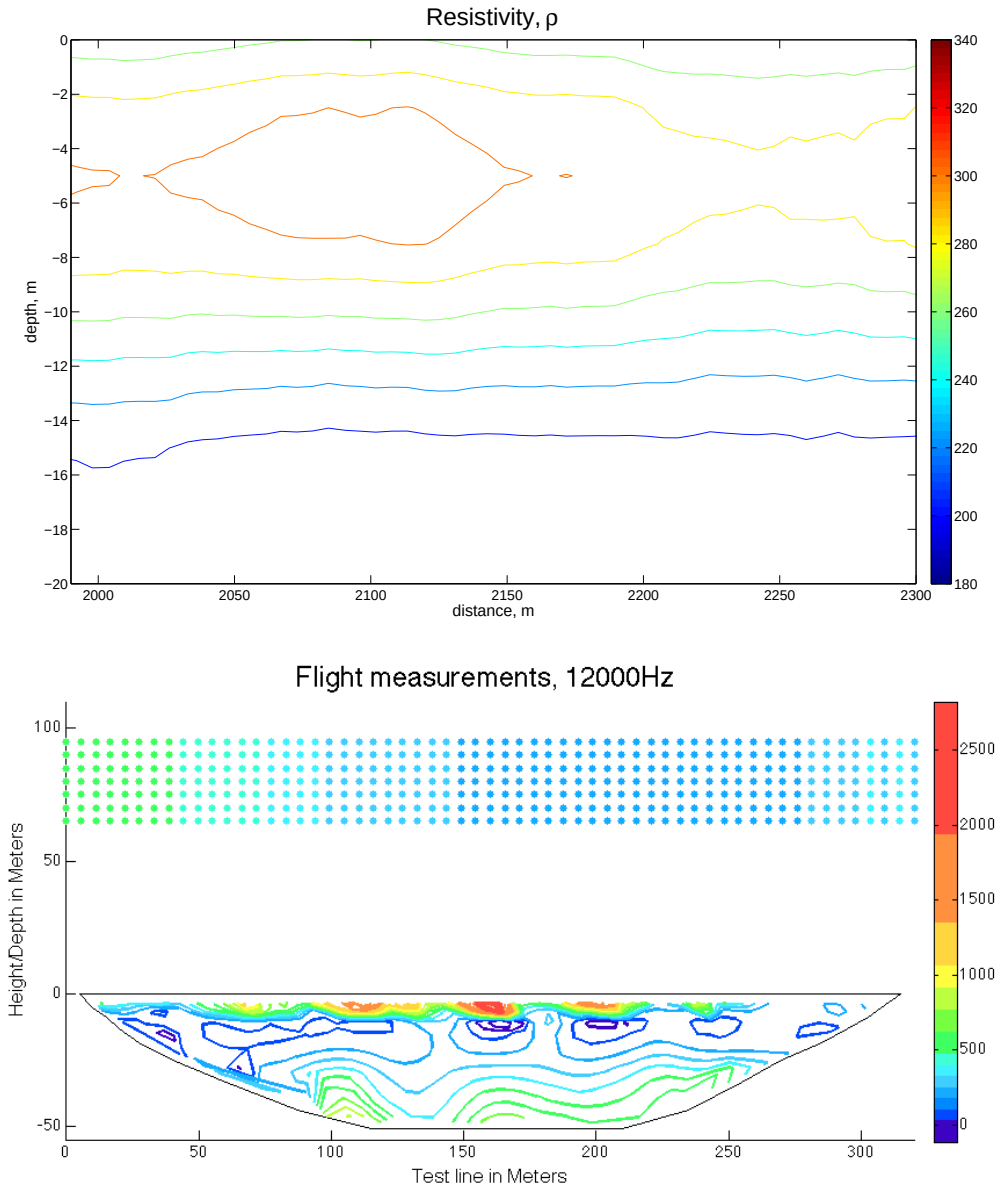

Figure 3.4: Reconstruction of resistivity (top) vs, the ground measurements (bottom) for the same segment of the test line

One should notice that the aerial and ground measurements are following the close, but not exactly the same path. At one point the ground measurements had to bypass the farm.

3.4 Remarks on optimization

There are two approaches to nonlinear optimization: *global algorithms* and *local algorithms*. The trade-off is the straightforward implementation and the high speed of the local algorithms, but possible convergence to the local rather than global minimum. However, this problem could at least partially resolved by using a good inital guess and a proper choice of the optimisation parameter and constraints.

Two particular methods are worth attention for the future analysis: the subspace trust-region nonlinear optimization based on the interior-reflective Newton method [16], which is considered the most efficient local method for constrained optimization and a simulated annealing algorithm, which is a global probabilistic approach [17].

The standard choice of the unknown variable in literature is either conductivity or resistivity. We suggest a different approach that has proven itself in nano-optics. We propose to set a vector of deviations from the average conductivity δ as an unknown. The final result is a distribution of δ normal to the measurement surface starting from the measurement point. A novelty in the choice of the optimization parameter is a possibility to shift it in both positive and negative directions, which significantly improves the convergence properties of the algorithm. The actual values of the conductivity are given by $\sigma + \delta$. The same approach could be also applied to resisitivity.

3.5 Full 3D inversion

3.5.1 Modeling the forward problem

In our analysis, we consider the paper [10] and references therein as a basis for the 3D inversion. The results reported in paper are very convincing, the output of the 3D inversion using moving footprints clearly appears to be much more accurate than a holistic inversion or a layered earth inversion. The authors used five different frequencies instead of four, however, it is a technical issue that can be resolved.

The notations are analogous to the ones in [10] and [18]. The conductivity $\sigma(r)$ ($r \in \mathbb{R}^3$) is defined as

$$\sigma(r) = \sigma_b(z) + \Delta\sigma(r),$$

where $\sigma_b(z)$ is the background conductivity, and $\Delta\sigma(r)$ is the anomalous conductivity. In general, we consider the vector Helmotz equation

$$(\nabla^2 + k^2)E = -i\omega\mu(J_0 + J_s), \quad \text{where} \quad k^2 = i\omega\mu(\sigma - i\omega\varepsilon). \tag{3.11}$$

In the above equation:

- E is the electric field,
- ε is the permittivity (again: $\varepsilon = \varepsilon_b + \Delta\varepsilon$),
- μ is the permeability,
- ω is the angular frequency,
- J_0 is an applied current density,
- $J_s = (\Delta\sigma - i\omega\Delta\varepsilon)E$.

Comparing the formulas in [18] and [10], it seem that the latter assumes $\varepsilon = 0$. Rewriting

$$E(r) = E^s(r) + E^b(r), \tag{3.12}$$

where E^s is the scattered electric field, and E^b is the background electric field, we can give the following expression for the solution of (3.11):

$$E(r) = E^b(r) + \int_\nu \Gamma(r, r')\Delta\sigma(r')E(r')d^3r',$$

where ν is a volume of interest, and Γ is the electric Green's tensor. By applying the method of moments, i.e., after choosing a proper set of basis functions to approximate E^s, the vector of the unknown coefficients $\mathbf{E}^s$ of E^s with respect to the chosen basis is given by

$$\mathbf{E}^s = (\mathbf{I} - \boldsymbol{\Gamma}\boldsymbol{\Delta\sigma})^{-1}\boldsymbol{\Gamma}\boldsymbol{\Delta\sigma}\mathbf{E}^b,$$

where $\mathbf{I}$ is the identity matrix, $\boldsymbol{\Gamma}$ is the matrix of the volume-integrated Green's functions, $\boldsymbol{\Delta\sigma}$ is a diagonal matrix of anomalous conductivities, and $\mathbf{E}^b$ is the vector of the coefficients of E^b.

3.5.2 The electric Green tensor

By definition, the electric Green's tensor $\Gamma(r, r')$ is obtained by solving

$$(\nabla^2 + k^2)\Gamma(r, r') = -i\omega\mu\delta(r - r')\mathbf{I}_3,$$

where $\delta(r - r')$ is the Dirac distribution, and $\mathbf{I}_3$ is the 3×3 identity matrix. Component-wise, we can write

$$(\nabla^2 + k^2)\Gamma_{i,j}(r, r') = -i\omega\mu\delta(r - r')\boldsymbol{\delta}_{i,j},$$

where $\Gamma_{i,j}(r, r')$ indicates the ith component of the Green's tensor at observation point r due to a unit point dipole at r' oriented in the jth direction (in the following, instead of i, j we will use a combination of x, y, z), and $\boldsymbol{\delta}_{i,j}$ is the Kronecker delta.

Following the derivations in [18] for the three-layer case, we express the tensor elements with respect to the cylindrical coordinates (i.e., $r = (\rho, \phi, z)$ and $r' = (\rho', \phi', z')$). Not to overload the equations, we will use the following notations:

- $\alpha_k = \sigma_k - i\omega\varepsilon_k$;
- $k_k^2 = i\omega\mu_k(\sigma_k - i\omega\varepsilon_k)$ (as before);
- $c = {}^{(\exp(-i\omega t)}/_{4\pi)}{}^{p}/_{|p|}$ (${}^{p}/_{|p|}$ is a unitary point current dipole);
- $s_k = (\lambda^2 - k_k^2)^{1/2}$;
- p_k and q_k represent the upward and downward propagating waves, respectively;
- the definition of ζ_k and η_K is more cumbersome, so we refer to [18];
- $X_k = \exp[s_k(z - z')]$;
- $K_k(\lambda, z, z') = (s_k\zeta_k - \lambda p_k)X_k - (s_k\eta_k + \lambda q_k)X_k^{-1} - \lambda Q_j$;
- $Q_j = \boldsymbol{\delta}_{i,j}{}^{c\lambda}/_{s_j \exp(-s_j|z-z'|)}$ ($\boldsymbol{\delta}_{i,j}$ is the Kronecker delta);
- J_i is the ith Bessel function;
- $t = {}^{z-z'}/_{|z-z'|}$.

Then, at the kth layer,

$$
\begin{aligned}
\Gamma_{x,x}^k(z, r') &= \beta_k \int_0^\infty \left[p_k X_k + q_k X_k^{-1} + Q_j\right] J_0(\lambda\rho')d\lambda \\
&\quad + \frac{\cos^2(\phi')}{2\alpha_k} \int_0^\infty K_k(\lambda, z, z') \left[J_0(\lambda\rho') - J_2(\lambda\rho')\right] \lambda d\lambda \\
&\quad + \frac{\sin^2(\phi')}{\rho\alpha_k} \int_0^\infty K_k(\lambda, z, z') J_1(\lambda\rho')d\lambda \,; \\
\Gamma_{y,x}^k(z, r') &= \frac{\sin(2\phi')}{4\alpha_k} \int_0^\infty K_k(\lambda, z, z') \left[J_0(\lambda\rho') - \frac{2}{\lambda\rho'} J_1(\lambda\rho') - J_2(\lambda\rho')\right] \lambda d\lambda \,; \\
\Gamma_{z,x}^k(z, r') &= -\frac{\cos(\phi')}{\alpha_k} \int_0^\infty \left|(\lambda\zeta_k - s_k p_k)X_k + (\lambda\eta_k + s_k q_k)X_k^{-1} + s_k t Q_j\right| J_1(\lambda\rho')\lambda d\lambda \,,
\end{aligned}
$$

$$
\begin{aligned}
\Gamma_{x,y}^k(z, r') &= \Gamma_{y,x}^k(z, r') \,; \\
\Gamma_{y,y}^k(z, r') &= \beta_k \int_0^\infty \left[p_k X_k + q_k X_k^{-1} + Q_j\right] J_0(\lambda\rho')d\lambda \\
&\quad + \frac{\sin^2(\phi')}{2\alpha_k} \int_0^\infty K_k(\lambda, z, z') \left[J_0(\lambda\rho') - J_2(\lambda\rho')\right] \lambda d\lambda \\
&\quad + \frac{\cos^2(\phi')}{\rho\alpha_k} \int_0^\infty K_k(\lambda, z, z') J_1(\lambda\rho')d\lambda \,; \\
\Gamma_{z,y}^k(z, r') &= -\frac{\sin(\phi')}{\alpha_k} \int_0^\infty \left|(\lambda\zeta_k - s_k p_k)X_k + (\lambda\eta_k + s_k q_k)X_k^{-1} + s_k t Q_j\right| J_1(\lambda\rho')\lambda d\lambda \,,
\end{aligned}
$$

and

$$\begin{aligned}
\Gamma^k_{x,z}(z,r') &= \frac{\cos(\phi')}{\alpha_k}\int_0^\infty \left[f_k X_k - g_k X_k^{-1} - tQ_j\right] J_1(\lambda\rho')s_k\lambda d\lambda\,;\\
\Gamma^k_{y,z}(z,r') &= \tan(\phi')\Gamma_{xz}\,;\\
\Gamma^k_{z,z}(z,r') &= \alpha_k^{-1}\int_0^\infty \left[f_k X_k + g_k X_k^{-1} + Q_j\right] J_0(\lambda\rho')\lambda^2 d\lambda\,.
\end{aligned}$$

3.5.3 Iterative Methods

We now describe some iterative methods that are commonly employed to solve the systems

$$\underbrace{(\mathbf{I}-\mathbf{\Gamma\Delta\sigma})}_{A}\underbrace{\mathbf{E}^s}_{x} = \underbrace{\mathbf{\Gamma\Delta\sigma E}^b}_{b} \tag{3.13}$$

or

$$\underbrace{(\mathbf{I}-\mathbf{\Gamma\Delta\sigma})}_{A}\underbrace{\mathbf{E}}_{x} = \underbrace{\mathbf{E}^b}_{b}. \tag{3.14}$$

We remark that, thanks to (3.12), (3.13) and (3.14) are equivalent. Since the above system comes from the discretization of a Fredholm integral equation, it is usually full.

In general, let us consider the common formulation

$$Ax = b, \quad A \in \mathbb{R}^{N\times N} \tag{3.15}$$

for both the systems (3.13) and (3.14). In the following, we list some efficient iterative methods that can be used to solve (3.15). They are all projection methods, i.e., at the mth iteration, two subspaces $\mathcal{P}_m,\ \mathcal{Q}_m \subset \mathbb{R}^N$ are chosen, and the conditions

$$x_m \in x_0 + \mathcal{P}_m$$

on the current approximate solution, and

$$r_m = r_0 - Ax_m \perp \mathcal{Q}_m$$

on the current residual, are enforced. In the above relations, x_0 is an initial guess for the solution, and r_0 is the associate residual; if no initial approximation for the solution is available, one just takes $x_0 = 0$. We underline that the inclusion of a meaningful initial guess $x_0 \neq 0$ usually results in a faster convergence (we refer to [9] for some guidelines on the choice of x_0). We focus on Krylov subspace methods, which are popular projection methods having as $\mathcal{P}_m$ and $\mathcal{Q}_m$ two Krylov subspaces. Given a square matrix C and a vector d, a Krylov subspace $\mathcal{K}_m(C,d)$ is defined by

$$\mathcal{K}_m(C,d) = \mathsf{span}\{d, Cd, \ldots, C^{m-1}d\}.$$

Different Krylov subspace methods are defined by taking different choices for $\mathcal{K}_m(C, d)$. For a complete description of most of them, we refer to [19] and [20], and the references therein.

- **Conjugate Gradient method (CG)**. Can be only applied to systems (3.15) having a Hermitian positive definite coefficient matrix. Referring to the general framework explained above, at the mth iteration,
$$\mathcal{P}_m = \mathcal{Q}_m = \mathcal{K}_m(A, r_0).$$

- **Conjugate Gradient method for the normal equations (CGNR)**. It is basically the CG method applied to the normal equations
$$A^*Ax = A^*b,$$
where A^* denotes the complex conjugate transpose of A. Therefore, at the mth iteration
$$\mathcal{P}_m = \mathcal{Q}_m = \mathcal{K}_m(A^*A, A^*r_0).$$

- **BiConjugate Gradient method (BiCG)**. Referring to the general framework explained above, at the mth iteration,
$$\mathcal{P}_m = \mathcal{K}_m(A, r_0) \quad \text{and} \quad \mathcal{Q}_m = \mathcal{K}_m(A^*, r_0)\,.$$

- **Variations of the BiCG**. We list the **Conjugate Gradient Squared (CGS)** (which does not require A^*) and the **BiConjugate Gradient stabilized (BiCGstab)** (which "smoothes" the behavior of the residual associated to the BiCG).

- **Generalized Minimal Residual method (GMRES)**. Referring to the general framework explained above, at the mth iteration,
$$\mathcal{P}_m = \mathcal{K}_m(A, r_0) \quad \text{and} \quad \mathcal{Q}_m = A\mathcal{K}_m(A, r_0)\,.$$
One drawback of GMRES is that the number of vectors to be stored is proportional to the number of iterations. To overcome this issue, restarting strategies are usually considered, and the corresponding methods are called GMRES(s), meaning that a restart happens after s iterations. The **Complex Generalized Minimal Residual method (CGMRES)** is generally employed when the system (3.15) comes from the discretization of an operator equation in a complex Hilbert space. It has been proved that the method converges if $\exists\gamma > 0$ such that
$$|x^*Ax| \geq \gamma(x^*x), \quad \forall x.$$

The convergence of the iterative methods above described can be accelerated by employing suitable

preconditioning. Basically, one solves

$$\underbrace{M_1 A M_2}_{\widetilde{A}} \widetilde{x} = \underbrace{M_1 b}_{\widetilde{b}} \tag{3.16}$$

instead of (3.15), and takes $x = M_2^{-1}\widetilde{x}$. M_1 and M_2 are called left and right preconditioners, respectively. They are effective if the condition number of $\widetilde{A}$ is lower than the condition number of A. The preconditioned version of the Krylov subspaces methods above listed is obtained by replacing A and r_0 with $\widetilde{A}$ and $\widetilde{r}_0 = \widetilde{b} - M_1 A x_0$, respectively. A very successful pair of preconditioners to be employed in connection with system (3.14) is described in [9]: one takes

$$\begin{aligned} M_1 &= \sqrt{\mathsf{Re}(\boldsymbol{\sigma}^b)}\,, \\ M_2 &= \left(2\sqrt{\boldsymbol{\sigma}^b}\right)\left(2\mathsf{Re}(\boldsymbol{\sigma}^b) + \boldsymbol{\Delta\sigma}\right)^{-1}\,, \end{aligned}$$

where $\boldsymbol{\sigma}^b$ and $\boldsymbol{\Delta\sigma}$ are the diagonal matrices of the background and the anomalous conductivities, respectively.

3.5.4 Computational costs of 3D algorithm

In terms of computational complexity, using performance time measurements in [10] and considering the larger dataset covereing most of Ireland, one arrives at 20-40 hours on a computer cluster belonging to the School of Mathematical Sciences at UCD using parallelized code in a compiled language. This number is of course subject to a large degree of uncertainty, probably up to one order of magnitude, it is however clear that a sequential implementation is not feasible.

Bibliography

[1] H. Huang, D. C. Fraser, Inversion of helicopter electromagnetic data to a magnetic conductive layered earth. *Geophysics*, 68(4), pp. 1211-1223, 2003. doi: 10.1190/1.1598113

[2] D. C. Fraser, Resistivity mapping with an airborne multicoil electromagnetic system. *Geophysics*, 43, pp. 144-172, 1978.

[3] H. Huang, D. C. Fraser, Mapping of the resistivity, susceptibility, and permittivity of the earth using a helicopter-borne electromagnetic system. *Geophysics*, 66, pp. 148-157, 2001.

[4] D. V. Fitterman, M. Deszcz-pan, Helicopter EM mapping of saltwater intrusion in Everglades National Park, Florida. *Explorational Geophysics*, 29, pp. 240-243, 1998.

[5] K. P. Sengpiel, B. Siemon, Advanced inversion methods for airborne electromagnetic exploration. *Geophysics* 65, pp. 1983-1992, 2000.

[6] S. L. Holladay, N. Valleau, E. Morrison, Application of multifrequency helicopter electromagnetic survey to mapping of sea-ice thickness and shallow-water bathymetry, in *G. J. Palacky, Ed., Airborne resistivity mapping*, Geological Survey of Canada, Paper 86-22, pp. 91-98, 1986.

[7] N. R. Paterson, S. W. Reford, Inversion of airborne electromagnetic data for overburden mapping and groundwater exploration, in *G. J. Palacky, Ed., Airborne resistivity mapping*, Geological Survey of Canada, Paper 86-22, pp. 39–48, 1986.

[8] W. Qian, et al., Inversion of airborne electromagnetic data using an Occam technique to resolve a variable number of layers, *in Proceedings of high-resolution geophysics workshop, SAGEEP*, pp. 735744, 1997.

[9] G. Hursan, M. S. Zhdanov. Contraction integral equation method in three-dimensional electromagnetic modeling. *Radio Science*, 37 (6), 2002. doi:10.1029/2001RS002513.

[10] L. H. Cox, G. A. Wilson, M. S. Zhdanov. 3D inversion of airbone electromagnetic data using a moving footprint. *Exploration Geophysics* 41, pp. 250–259, 2010.

[11] F. C. Frischknecht, Fields about an oscillating magnetic dipole over a two-layer earth and application to ground and airborne electromagnetic surveys. *Quarterly of the Colorado School of Mines*, 62(1), 1967.

[12] S. H. Ward, Electromagnetic theory for geophysical applications, *in S. H. Ward, Ed., Mining geophysics, 2, Theory*, Society for Exploratory Geophysics, pp. 13-196, 1967.

[13] S, H. Ward, G. W. Hohmann, Electromagnetic theory for geophysical applications, *in M. N. Nabighian, Ed., Electromagnetic methods in applied geophysics, 1, Theory*, Society for Exploratory Geophysics, pp. 130 311, 1988.

[14] M. Born, E. Wolf, *Principles of Optics*, 7th ed., Cambridge University Press, Cambridge, UK, 1999

[15] D-Q Zhou et al, Inversion of frequency domain helicopter-borne electromagnetic data with Marquardt's method. *Chinese Journal of Geophysics*, 53(1), pp. 189–197, 2010

[16] T. F. Coleman, Y. Li, On the convergence of interior-reflective Newton methods for nonlinear minimization subject to bounds, Mathematical Programming 67, 189-224, 1994.

[17] J. Haddock , J. Mittenthal, Simulation Optimization Using Simulated Annealing Computers and Industrial Engineering, 22(4), 387-95, 1992

[18] A. P. Raiche. An integral equation approach to three-dimensional modeling. *Geophys. J. R. astr. Soc.*, 36, pp. 363-376, 1974.

[19] Y. Saad. *Iterative Methods for Sparse Linear Systems*, 2nd. Ed SIAM, 2003.

[20] H. van der Vorst. *Iterative Krylov Methods for Large Linear systems*. Cambridge University Press, 2003.